scientific reports

Check for updates

OPEN

Synergetic and alone influence of graphite platelet and SiC on the oxidation resistance of ZrB_2 ceramics

Hamze Ghanbari Nezhad & Zohre Balak✉

This study investigates how adding graphite platelets (G_P), with and without SiC, affects the oxidation resistance of ZrB_2 ceramics. The specimens—ZrB_2-10G_P, ZrB_2-15G_P, ZrB_2-15SiC, ZrB_2-30SiC, ZrB_2-30SiC-10G_P, and ZrB_2-30SiC-15G_P—were sintered at 1850 °C for 8 min via spark plasma sintering (SPS). For oxidation evaluation, the samples were exposed to air in the furnace at a temperature of 1450 °C for different times (30, 60, 90, 120, 180, 300 min). Also, the simultaneous thermogravimetric analysis (TGA) and differential thermal analysis (DTA) up to 1200 °C were applied to investigate the in situ oxidation. FESEM and EDS were utilized to perform microstructural and elemental analyses on the cross-sections of various oxide layers. It was disclosed that the G_P and SiC both improve the oxidation resistance. The best oxidation resistances were obtained in the ZrB_2-30SiC and ZrB_2-30SiC-10G_P with the lowest oxidation layer thicknesses of 38 ± 3 µm and 40 ± 4 µm, respectively. Also, the lowest oxidation resistance was obtained in pure ZrB_2 with the highest oxide layer thickness of 129 ± 5 µm. The formation of an adherent oxide layer is the dominant factor for improving the oxidation resistance. The oxidation mechanism of all samples except ZrB_2 was diffusion oxygen-controlled with a parabolic behavior. Also, TGA and DTA analysis showed a mass loss at the initial stage (∼ 200°C), followed by mass gain at 709 °C and 1065°C.

Keywords ZrB_2-SiC, Graphite platelets, SPS, Oxidation resistance, Parabolic

Zirconium diboride (ZrB_2) is a binary compound of zirconium and boron, which belongs to Ultra High Temperature Ceramics (UHTCs); it is characterized by its high melting point (3224 °C), excellent hardness, and remarkable thermal and electrical conductivity. Due to these unique properties, ZrB_2 has garnered significant attention in various applications such as re-entry vehicles and aerospace[1,2], furnace electrodes, microelectronics, cutting tools, metal crucibles, and solar collectors[3].

Of course, one of the main challenges for the use of ZrB_2 at high temperatures is its weak oxidation resistance; When ZrB_2 is exposed to air oxygen, it is oxidized according to Eq. (1) and causes the formation of ZrO_2 and B_2O_3 oxide layers.

$$ZrB_2 + 1/2\ O_2\ (g) = \ ZrO_2 + B_2O_3 \tag{1}$$

At temperatures around 1273 K, the protection of the oxide layer decreases due to the preferential oxidation of B_2O_3[4].

In the temperature range of 1373–1673 K, the evaporation of B_2O_3 accelerated[3,4] and led to form a porous ZrO_2 layer and finally to the linear oxidation of ZrB_2 substrate[4].

To solve this problem, in recent years, various additives have been added to this ceramic in different amounts, such as SiC, $MoSi_2$, VC[5], Si_3N_4 [3], HfB_2, and graphite[6,7].

The dense ultrahigh-temperature ZrB_2–15 vol.% SiC–5 vol.% WC ceramics were created through hot pressing at 2050 °C and 30 MPa. High-temperature oxidation resulted in to formation of a three-layer scale consisting of borosilicate glass, ZrO_2 with other oxides (WO_3 and SiO_2), and boron and silicon-depleted materials. After oxidation at 1500 °C for 50 h, the scale was 85 µm thick, while at 1600°C for 2 h, it measured 84 µm. The dense scale enabled the material to retain 70% of its strength after oxidation at 1500°C and 50% after oxidation at 1600 °C, outperforming the base ceramics[8].

Department of Materials Science and Engineering, Ahv.C, Islamic Azad University, Ahvaz, Iran. ✉email: zbalak@iau.ac.ir

Sintering ZrB_2-$MoSi_2$ ceramics at 1900–2150 °C results in beneficial microstructures with (Zr, Mo)B_2 solid solutions, improving performance during cyclic oxidation at 1650 °C. It revealed an interpenetrating microstructure of ZrO_2 micro-grains and nano-sized MoB particles, which effectively limits oxygen penetration to a few microns[9].

Nils-Christian Petry[10]showed that polymer-derived ceramics enhance the high-temperature oxidation resistance of ZrB_2-based monoliths. They coated the ZrB_2 powder with SiCN, SiZrCN, or SiZrBCN and densified it at 1800 °C. Thermogravimetric analysis (TGA) at 1300°C assessed oxidation kinetics over 50 and 100 h. Results showed improved oxidation resistance compared to ZrB_2–SiC.

In our previous study[11], the oxidation resistance of ZrB_2-SiC-based composites in the presence of various additives was investigated. Nine factors, including the contents of SiC, Cf, $MoSi_2$, HfB_2, and ZrC, as well as milling time and SPS parameters (temperature, time, pressure), were analyzed using the Taguchi design method. Oxidation tests were conducted at 1600 °C for 1 h. Results showed that ZrC negatively impacts oxidation resistance, while HfB_2 has a positive effect. Temperature was the most influential SPS parameter, while pressure and milling time had minimal effects. Other factors contributed varying percentages to oxidation resistance, with SiC being the most significant contributor at 12.8%.

Among the different additives, SiC is one of the best additives that not only improves oxidation resistance but also improves sintering ability, hardness, fracture toughness, bending strength, and shock resistance. Therefore, in this article, ZrB_2-SiC composite was chosen as the base composite. Also, due to the positive influence of graphite on the oxidation resistance, it was chosen as reinforcement. The effect of graphite amount on the oxidation resistance of ZrB_2-SiC composite at 1450 °C was investigated.

Experimental

Commercial SiC (25 µm particle size, 98.7% purity), and ZrB_2 (20 µm particle size, 99.5% purity) powders (were sourced from the Northwest Institute for Non-Ferrous Metal Research (China)) as well as G_p (C > 99.9%, platelet diameter of 5–10 µm, US Research Nanomaterials, Inc.) were used as the initial materials. Eight composite samples were created based on the compositions and spark plasma sintering conditions outlined in Table 1. The powders were weighed and mixed using wet ball milling for 3 h at 250 rpm in ethanol, utilizing tungsten carbide cups and balls. After drying the powder mixtures on a magnetic heater, they were placed into graphite molds designed for sintering. The sintering process was conducted using spark plasma sintering technology (SPS: 20T-10, China) at 1850 ∘C for 8 min under 35 MPa pressure in a vacuum. The resulting disk-shaped composites were ground to eliminate any attached graphite foils and then machined using EDM technology for oxidation testing. The isothermal oxidation tests were performed in a box furnace (Azar Furnace, F64L, 1500 °C) at a constant temperature of 1450 °C for durations of 30, 60, 90, 120, 180, 300 min. Samples with the dimensions of 3*3*10 mm^3 were applied for isothermal oxidation resistance. The relative mass change, used as an oxidation criterion, was calculated by dividing the mass change due to oxidation by the initial mass. For this purpose, the mass of samples before and after the oxidation was measured via a balance with an accuracy of four decimal places (RADWAG AS 520.R2 PLUS).

The non-isothermal oxidation test of the thermogravimetric analyzer (STA 504, Bahr, Germany) was primarily conducted to identify the critical temperatures for oxidation and to monitor the mass changes during heating, providing insights into the early stages of oxidation. The sample (within a weight of 10 mg) was heated at a rate of 10 °C/min from 50 to 1200 °C in a flowing air environment.

Microstructural and elemental analyses were conducted using Tescan Mira3 FESEM equipped with EDS capabilities. Phase identification of oxidized samples was carried out by X-ray diffraction (XRD: Philips, PW 1730, operating at 40 kV and 30 mA).

Results and discussion

G_P effect

Phase identification and morphology of oxide scale

Figure 1 shows the typical XRD spectrum for Zr, Zr10G_P, and Zr15G_P samples after exposure to the air for 5 h at 1450 °C. It is worth noting that the XRD results of samples before oxidation were published in our previous works[12]. According to Fig. 1, it is revealed that the predominant phases in the microstructure of all samples are t-ZrO_2 and m-ZrO_2, which are formed by the oxidation of the ZrB_2 phase (Eq. 1) and are consistent with the results of previous research[4]. It is obvious that besides the ZrO_2, a few amount of B_2O_3 has been detected in the XRD results. This low B_2O_3 amount originates from its evaporation at the oxidation temperature of 1450 °C for

Sample code	ZrB_2 (vol%)	SiC (vol%)	G_P (vol%)	R.D%
Zr	100	–	–	81
Zr10G_P	90	–	10	93.8
Zr15G_P	85	–	15	98.9
Zr15Si	85	15	–	98.8
Zr30Si	70	30	–	92.6
Zr30Si10G_P	60	30	10	99.6
Zr30Si15G_P	55	30	15	100

Table 1. Chemical compositions, SPS conditions, as well as the relative density (R.D%) of all samples.

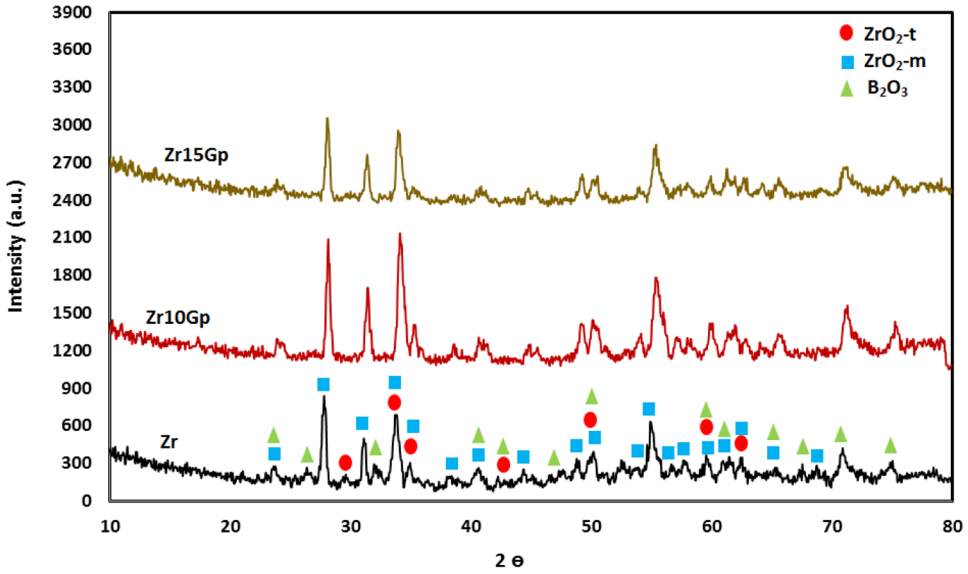

Pos. [°2Th.]	ZrO_2-m	B_2O_3	ZrO_2-t	Pos.[°2Th.]	ZrO_2-m	B_2O_3	ZrO_2-t
23.65	011	100	-	50.02	-220	104	220
26.42	-	101	-	52.63	-	-	-
27.768	-111	-	-	53.8	202	-	-
29.61	-	-	111	55.015	221	-	-
31.097	111	-	-	56.84	212	-	-
32.11	-	102	-	57.71	-131	-	-
33.754	002	-	002	59.59	131	203	311
34.89	020	-	200	61.28	113	105	-
38.29	012	-	-	62.41	-213	-	222
40.53	-211	103	-	65.23	-132	210	-
42.22	-	111	112	67.5	-	204	-
44.43	112	-	-	68.7	132	-	-
47.51	-	112	-	70.89	-	115	-
48.76	-212	-	-	74.81	-	213	-

Fig. 1. The XRD patterns of the Zr, $Zr10G_p$ and $Zr15G_p$ samples, as well as the peak positions and their crystalline planes.

5 h. Also, some peaks belonging to the B_2O_3 were omitted in $Zr10G_p$ and $Zr15G_p$ in comparison with Zr, which can be associated with the positive effect of graphite in removing oxide impurities.

Figure 2 presents the FESEM images of the cross-section for the monolithic ZrB_2 as well as ZrB_2 containing 10 and 15 vol% G_p after oxidation at 1450 °C for 5 h. The microstructure of all samples before oxidation is given in our previous works[12,13]. A three-layered structure can be distinguished through Fig. 2. According to the maps analysis for ZrB_2 containing 10 and 15 vol% G_p, which are given in Figs. 3 and 4, and their XRD results (Fig. 1), this layered structure consists of (1) a very thin layer of B_2O_3, (2) ZrO_2, and (3) an unaffected substrate. In all samples, ZrO_2 grains with a grey light color can be seen in the oxidized region.

Many cavities exist in the microstructure of each sample according to Fig. 2 (indicated with white arrows), which can be seen more clearly in the map analysis for ZrB_2 reinforced with 10 and 15 vol% G_p (Figs. 3 and 4). These cavities are introduced in the microstructure as the result of incomplete densification, which is discussed elsewhere[12,13] in detail, and evaporation of B_2O_3. ZrB_2 transits to ZrO_2 and B_2O_3 (l) through reaction (1) while it is exposed to air at a temperature of 1500 ∘C. According to the ZrB_2 volatility diagram[6] equilibrium pO_2 of 1.9×10^{-11} Pa ($\log pO_2 = -10.73$) is required for ZrB_2 oxidation. For $pO_2 < 1.9\times10^{-11}$ Pa, ZrB_2 will be in equilibrium with the vapor species such as B_2O_3, B_2O_2, BO, and B[6].

Since the vapor pressure of B_2O_3 (g) is much higher than any other species, it will preferentially vaporize as follows[14].

$$B_2O_3\,(l) \rightarrow B_2O_3\,(g) \tag{2}$$

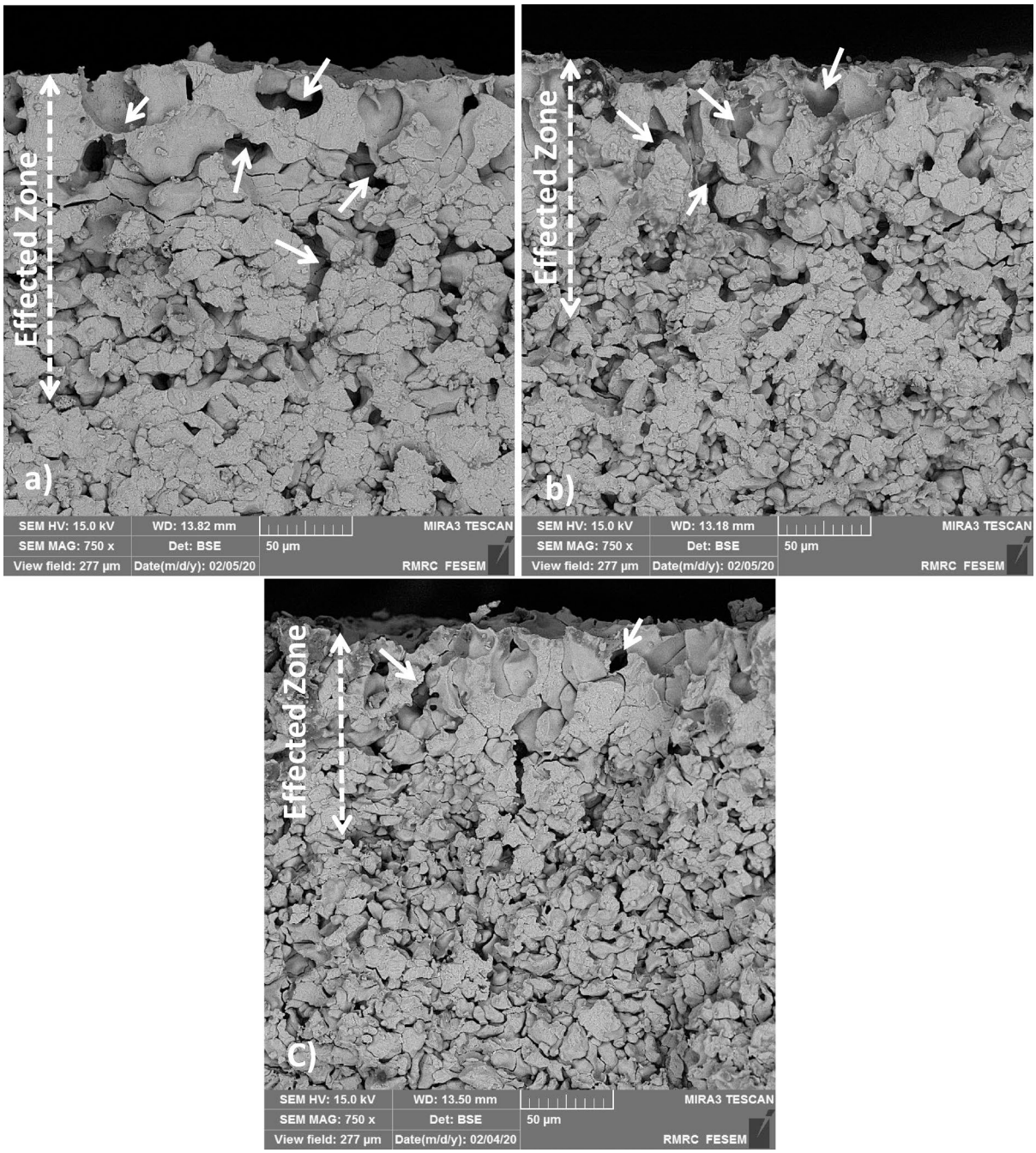

Fig. 2. FESEM images of cross-section of (**a**) Zr, (**b**) Zr10G_p and (**c**) Zr15G_p after oxidation for 5h at 1450 °C.

Once the B_2O_3 (g) can escape through the oxide scale, the voids can be created and lead to form a porous skeleton of ZrO_2. Of course, it may be that the B_2O_3 (g) with a high partial pressure of 2.7 *10^3 Pa, cannot exist quickly from the oxide scale; in this case, if its pressure overdue the ambient pressure, the air bubble may be created.

ZrB_2 containing 10 and 15 vol% G_p has a lower amount of voids with a smaller size (Fig. 1) compared with the free-G_p sample (Zr). In addition, by increasing the G_p amount from 10 to 15 vol%, the size and the amount of voids decrease, according to their maps analysis (Figs. 3 and 4). In other words, G_p improves the oxidation resistance of ZrB_2 by preventing the B_2O_3 evaporation (Eq. 2), through reaction (3) to some extent, and eventually reduces the creation of voids and bubbles. The thermodynamic calculation (conducted via HSC software) shows, reaction (3) occurs at 1600 °C due to its negative $\Delta G = -17.07$ kcal.

$$ZrO_2 + B_2O_3\,(l) + 5C = ZrB_2 + 5CO\ \ (g) \tag{3}$$

Comparing the elemental map analysis shows, the amount of B_2O_3 created in the microstructure decreases with graphite addition, which is completely consistent with the XRD result.

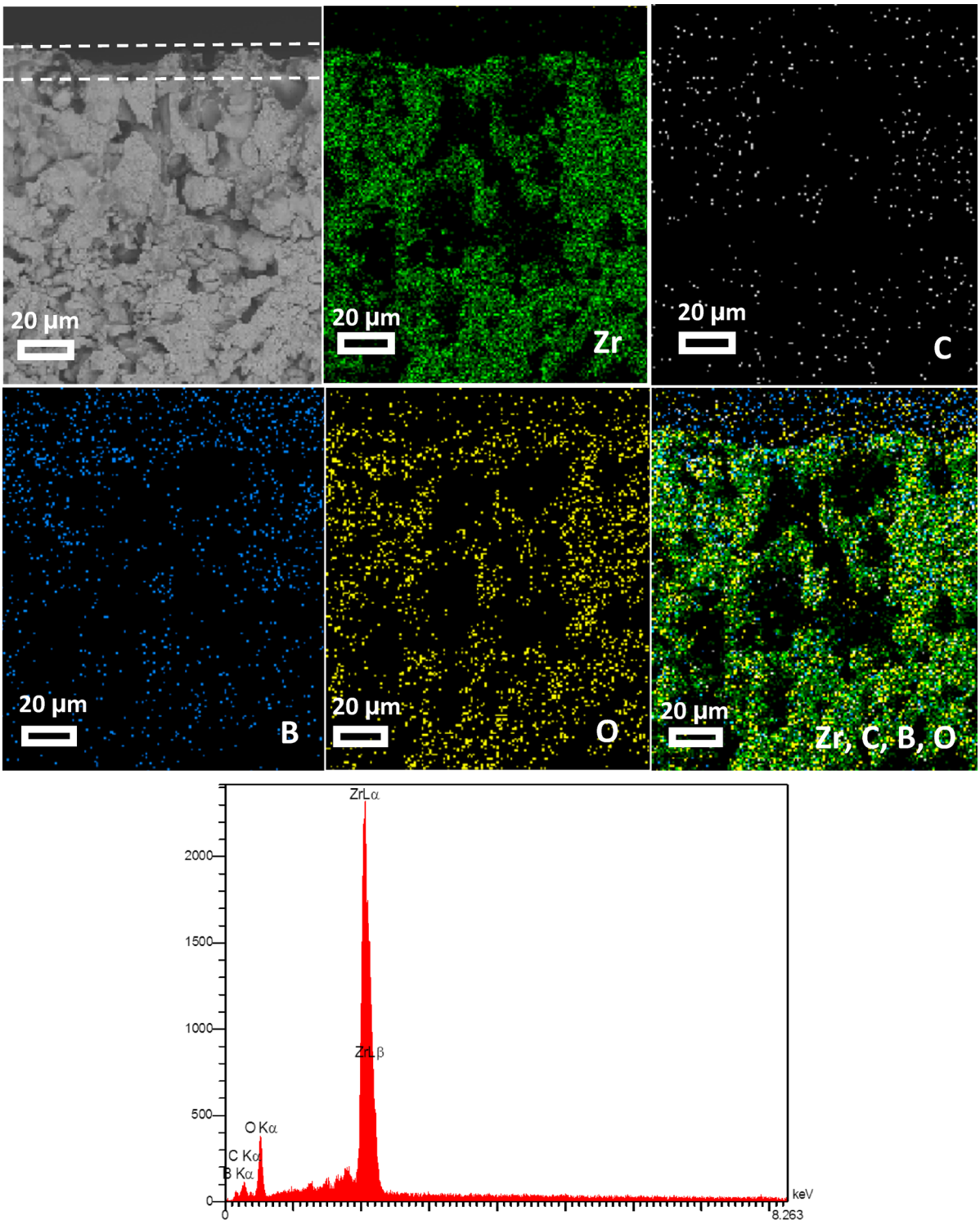

Fig. 3. Map analysis of the cross section of Zr10G_p after oxidation for 5 h at 1450 °C as well as its EDS profile.

Also, it is clear, the diffusion depth of oxygen decreases with G_p addition. In other words, graphite prevents the evaporation of B_2O_3 through the reaction (4) and eventually leads to a decrease in the cavities or air bubbles formation in the microstructure, which act as paths for oxygen diffusion. So, by increasing the graphite addition, the amount of porosity is decreased, and the FESEM images and elemental analysis maps (Figs. 2 and 4) confirm this issue.

In Fig. 5, the amount of weight change of all samples after oxidation at 1450 °C for 5 h is presented. It can be seen that with the addition of graphite, the amount of weight change has been significantly reduced, and it has improved the oxidation resistance.

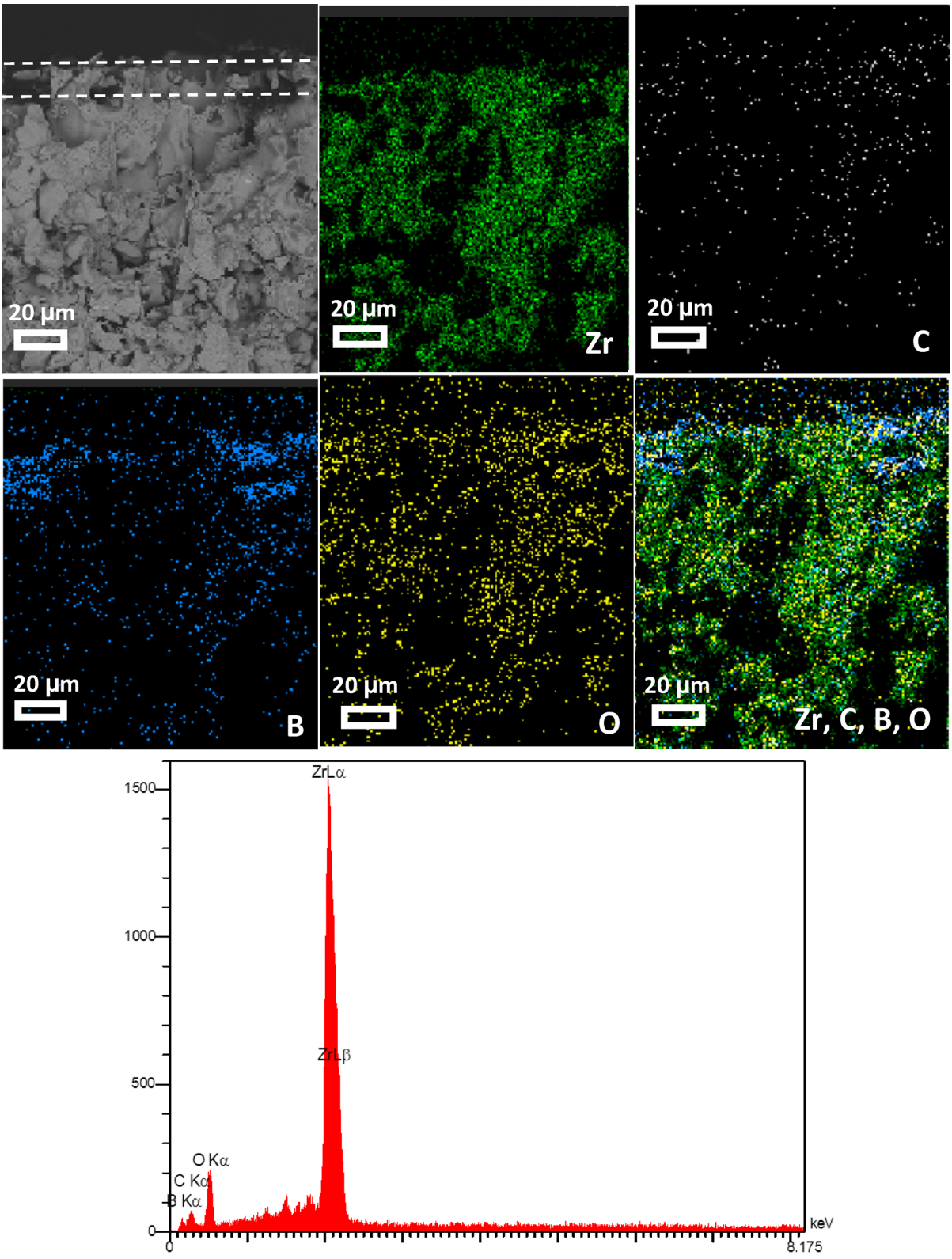

Fig. 4. Map analysis of the cross section of $Zr15G_p$ after oxidation for 5h at 1450 °C as well as its EDS profile.

As previously discussed, the positive effect of graphite on oxidation resistance is due to its reaction with boron oxide, preventing its evaporation and ultimately the formation of porosity in the microstructure.

According to the FESEM images, the thickness of the oxide layer was measured by Image J software and listed in Table 2. As seen, by addition of graphite, up to 10 vol% and 15 vol%, the thickness of the oxide layer decreases

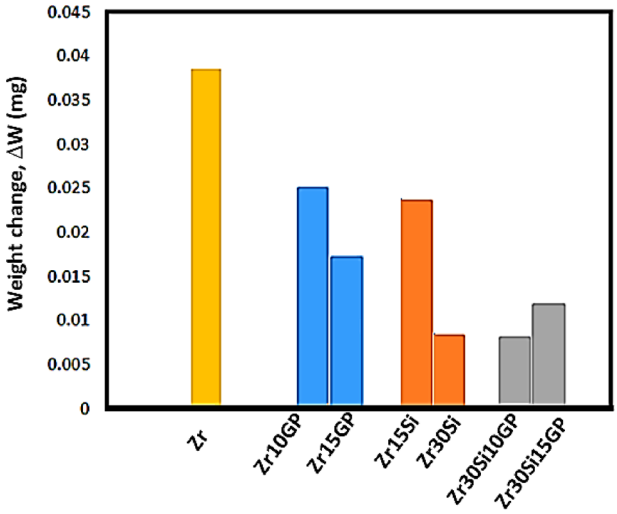

Fig. 5. The weight changes of all samples after oxidation at 1450 °C for 5 h.

Sample	Zr	Zr10G_p	Zr15G_p	Zr15Si	Zr30Si	Zr30Si10G_p	Zr30Si15G_p
Thickness, μm	129 ± 5	112 ± 5	80 ± 4	62 ± 5	38 ± 3	40 ± 4	64 ± 5

Table 2. Thickness of oxide layer after oxidation at 1450 °C for 5 h for all samples.

to 112 μm and 80 μm from 129 μm in the Zr sample, respectively. This confirms the weight loss results obtained for these samples (Fig. 5).

SiC content

In Fig. 6, the FESEM images of the cross section of the ZrB_2-15 vol% SiC and ZrB_2-30 vol% SiC composites after oxidation at 1450 °C are presented. The XRD result of ZrB_2-15 vol% SiC after oxidation at 1450 °C is given in Fig. 7. As seen, the key products formed during the oxidation of the composites include ZrO_2-m, SiO_2, and $ZrSiO_4$, which were formed during reactions (1), (4), and (5), respectively. It is clear that the $SiO_2 + B_2O_3$ layer plus the layer affected by oxidation in the sample containing 15 vol% % SiC (25 μm, 62 μm respectively) is more than the sample containing 30 vol% SiC (11 μm, 38 μm respectively) (Table 2). It discloses the enhancement in the oxidation resistance by increasing the amount of SiC. Also, according to Fig. 5, the weight changes after oxidation resistance at 1450 °C for 5 h, decrease noticeably in the presence of 15 vol% and 30 vol% SiC, which is completely following FESEM images.

$$SiC + 3/2O_2 = SiO_2 + CO \ \ (g) \tag{4}$$

$$ZrO_2 + SiO_2 = ZrSiO_4 \tag{5}$$

The ability to resist oxidation is determined by a protective oxide layer that forms on the surface of the matrices. In some situations, this resistance is influenced by the gas pressure within the internal oxide layer. At the temperature of 1450 °C, the vapor pressures for B_2O_3 and SiO_2 are roughly 100 Pa and 10^{-5} Pa, respectively, whereas ZrB_2 has a vapor pressure of just 10^{-9} Pa[15].

Due to its high vapor pressure, B_2O_3 is oxidized faster and, as mentioned before, either it leaves the matrix and causes porosity, or it remains in the matrix and causes bubbles. Due to the addition of SiC, the formed SiO_2 reacts with B_2O_3 and forms a sticky borosilicate layer, thus preventing the evaporation and removal of B_2O_3 and improving oxidation resistance. It can be seen that compared to the sample containing graphite, ZrB_2-Gr (Fig. 2), the microstructure of the sample is denser and lacks large pores. This issue indicates the more beneficial effect of SiC in comparison with the Gr addition.

Co-existence of SiC and G_P

According to Fig. 5 (the weight changes against chemical composition), the addition of 10 vol% graphite to the Z30Si sample does not significantly change the oxidation resistance, while adding more amounts (15 vol%) results in to reduction of oxidation resistance.

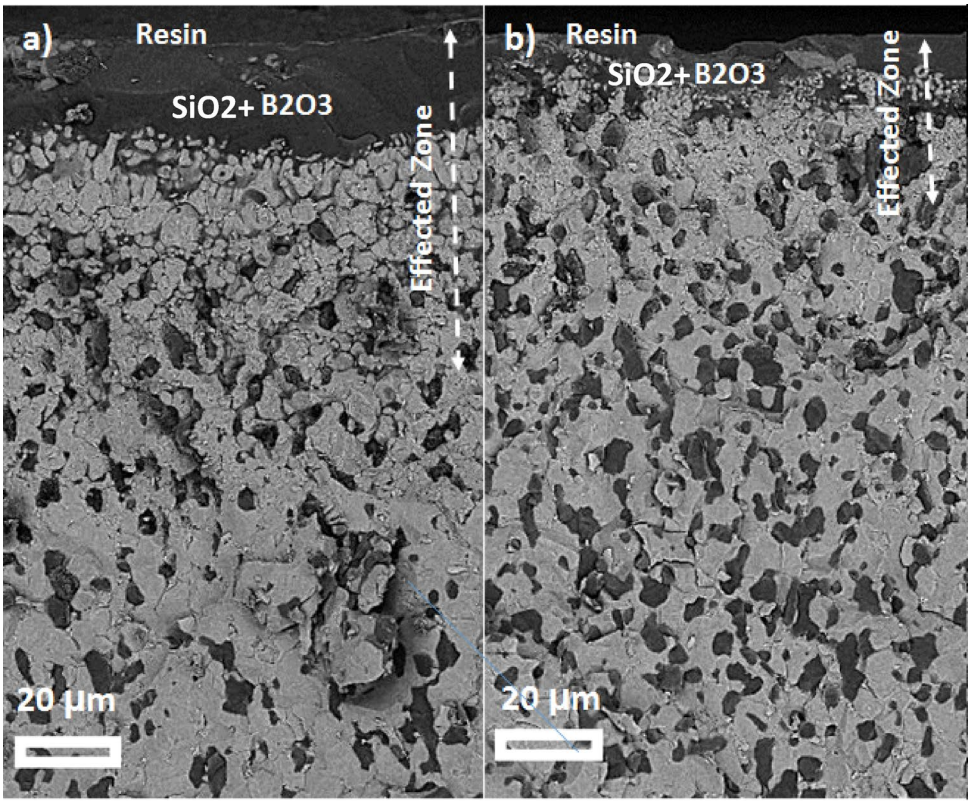

Fig. 6. FESEM images of the cross-section of ZrB_2-SiC composites, (**a**) 15vol%SiC and (**b**) 30 vol% SiC after oxidation for 5h at 1450 °C.

According to the previous research[6,16], it was reported that the graphite addition improves the oxidation resistance. The introduction of graphite into ZrB_2-SiC could alter the development of a SiC-depleted layer beneath the outer SiO_2-rich surface. Graphite boosts the carbon activity in comparison to nominally pure SiC, which is likely to impact the carbon monoxide pressure found beneath the SiO_2 layers. Consequently, the addition of carbon may reduce the vaporization of SiC due to the increased pressure of carbon monoxide. Thus, the overall carbon monoxide pressure in equilibrium with SiC under its outer SiO_2 layer is contingent on the carbon activity in the system. At around 1500 °C, studies have shown that the total pressure ($pSiO + pO_2$) can rise dramatically (approximately 100 times) for carbon-saturated silicon carbide in contact with silica, as opposed to nominally pure silicon carbide[6].

Jin et al.[16] reported that a new ZrB phase exists in the oxide layer of ZrB_2-SiC-G composite in addition to t-ZrO_2 and m-ZrO_2 during oxidation at 1500 °C and low oxygen partial pressure. It is presumably due to the incomplete oxidation.

Also, it was revealed through the oxidation time ascent, allotropic transformation occurred, and t-ZrO_2 will be transformed to m-ZrO_2 involuntarily, and ZrO_2 with the monoclinic structure was detected as the dominant phase. The t-ZrO_2 has a critical crystal size above which the allotropic transformation will occur. It was assumed, ZrB_2 oxidized to t-ZrO_2 through the reaction (1). Then, its crystal size grows by increasing the oxidation time, and it will be transformed to m-ZrO_2 when it exceeds the critical size[16,17].

The reason for the lack of positive effect of graphite addition on oxidation in the present study can be attributed to the high additive amounts of 40 vol% in Zr30Si10Gr (30 vol% SiC and 10 vol% Gr) and 45 vol% (30 vol% SiC and 15 vol% Gr). High amounts of additives make it difficult to distribute them uniformly in the matrix, thus causing microstructural inhomogeneity and reduced oxidation resistance.

In Fig. 8, the FESEM images of the cross-section of samples containing both graphite and SiC are given. It is clear; the microstructure is similar to ZrB_2-SiC samples (Fig. 6), especially for the Zr30Si rather than Zr15Si sample, and it consists of a B_2O_3 layer with the distributed ZrO_2 grains. According to these FESEM images, the thickness of the oxide layer was measured and listed in Table 2. As seen, firstly, with the addition of 10 vol% G_p, the thickness of the oxide layer does not change significantly; however, by increasing the G_p addition up to 15 vol%, it increases significantly to 64 ± 5 µm in Zr30Si15G_p from 40 ± 4 µm in Zr30Si10G_p. To investigate this issue,

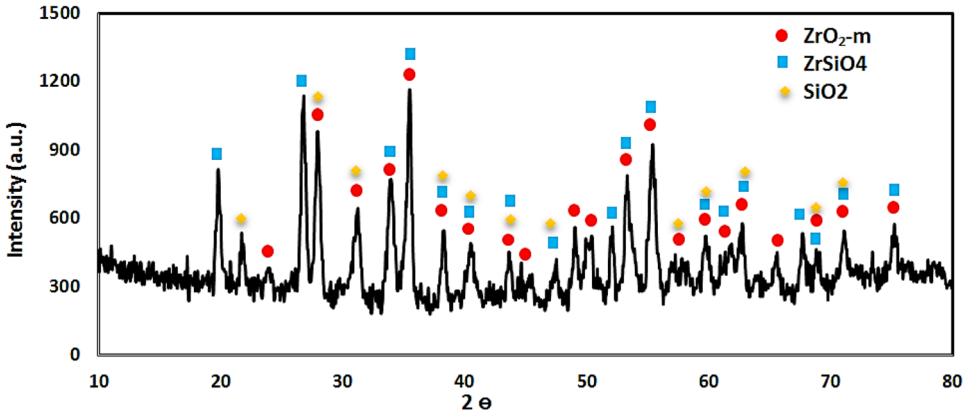

Pos.[°2Th.]	ZrO_2-m	$ZrSiO_4$	SiO_2	Pos. [°2Th.]	ZrO_2-m	$ZrSiO_4$	SiO_2
19.790	-	101	-	50.11	220	-	-
21.75	-	-	100	51.984	-	321	003
23.87	011	-	-	53.311	202	312	-
26.744	-	200	-	55.325	013	213	-
27.919	-111	-	011	57.55	-131	-	013
31.095	111	-	-	59.71	131	411	120
33.902	002	211	-	61.61	113	004	-
35.397	200	112	-	62.62	311	303	21-1
38.219	021	220	110	65.44	-132	-	-
40.46	-211	202	102	67.646	-	332	-
43.59	121	301	-	68.80	132	204	300
45.04	-202	-	-	71.03	321	422	203
47.35	-	103	201	75.13	041	224	-
48.991	-212	-	-	-	-	-	-

Fig. 7. The XRD pattern of the Zr15Si sample, as well as the peak positions and their crystalline planes.

the elemental map distribution of $Zr30Si15G_p$ is presented in Fig. 9. Oxygen has penetrated the microstructure to about 60 µm, which is consistent with the thickness of the oxidized layer reported in Table 2.

To investigate the in situ oxidation mechanism against temperature, the weight change and DTA curves for the $Zr30Si10G_p$ sample are presented in Fig. 10. It is observed that the weight of the sample decreases rapidly from about 200 °C to about 750 °C and then increases up to 1050°C. After that, it shows a decreasing behavior in the range of 1050–1065°C and finally continues to increase from 1065 to 1200 °C. The weight loss in the range of 200–750°C can be attributed to the G_p oxidation reaction, which causes the formation of carbon monoxide/carbon dioxide gases that are released from the system and cause the weight of the sample to decrease. After that, the weight increase from 750 to 1050°C can be attributed to the oxidation of ZrB_2 and the formation of B_2O_3 and ZrO_2, which the peaks identified in the DTA curve in this temperature range indicate and confirming the completion of this reaction. Next, in the temperature range of 1050–1065 °C, the partial weight loss observed is due to the evaporation reaction of B_2O_3, which causes weight loss due to the exit of B_2O_3 from the system. Finally, the continuous weight increase of the sample from 1065 to 1200 °C can be attributed to the oxidation of SiC and the formation of SiO_2. The formation of SiO_2 causes weight increase both due to the formation of an oxide scale and due to the reaction with B_2O_3 and the formation of a borosilicate layer, and in the prevention of B_2O_3 evaporation.

Malik et al.[18] reported continuous mass gain (with two sharp increases at 740 °C and 1180 °C) in ZrB_2-20 vol% SiC oxidized from 50 to 1300 °C during TGA analysis. The result of this research (mass gain with two sharp increases at 709 °C and 1065 °C) is completely consistent with them. The difference in weight changes in the initial stages (from 50 °C to around 740 °C) between the present study and the reference [18] is due to the presence of G_p in the present study, as previously discussed.

Oxidation resistance

In Fig. 11, the weight change curves as a function of oxidation time at a temperature of 1450 °C for all samples are presented. It is clear that for all samples (except pure ZrB_2, Zr), the weight change-temperature curves have two distinct regions: 1) a linear curve and 2) a nearly smooth curve.

As observed in Fig. 11, the weight change rate over time decreases for all samples except pure ZrB_2 (Zr) as time increases. In linear and parabolic oxidation mechanisms, the weight change rate exhibits an ascending and

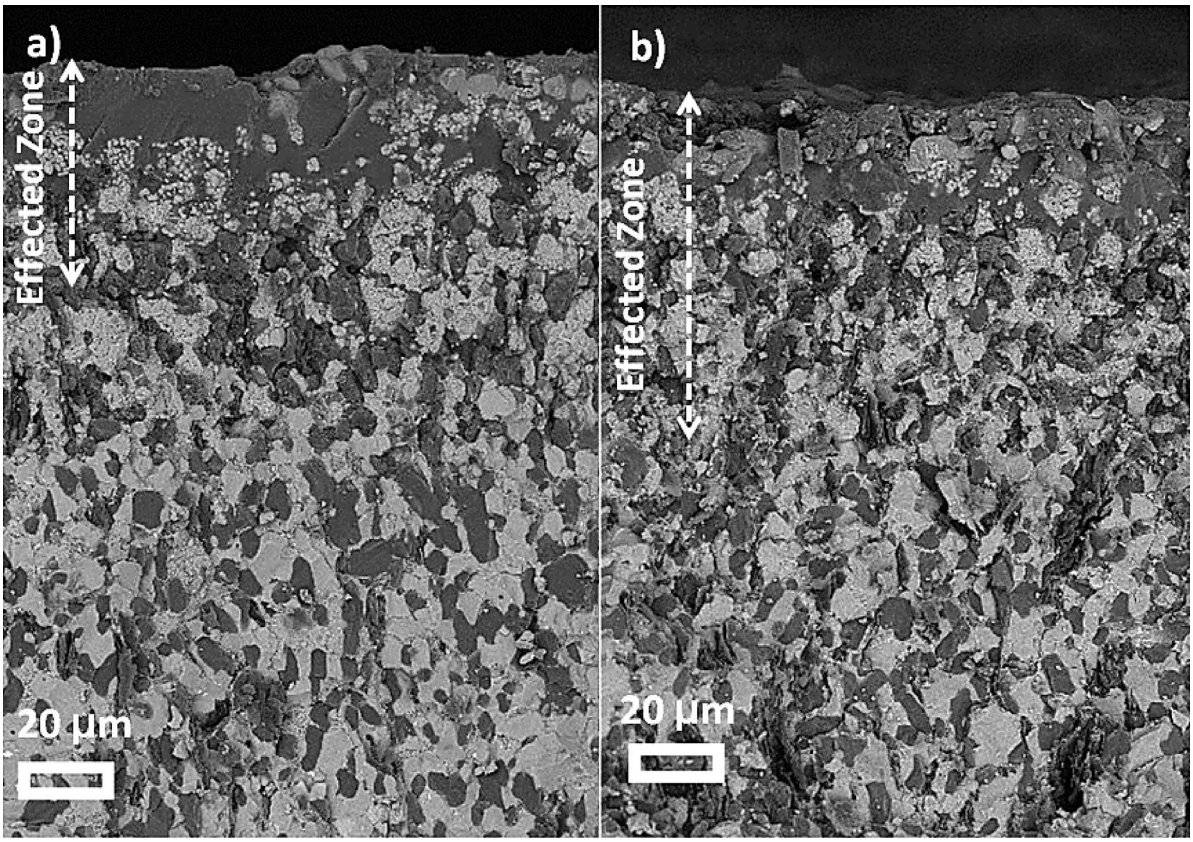

Fig. 8. FESEM images of cross-section of ZrB_2-SiC-G_p composites, (**a**) 10vol%G_p and (**b**) 15 vol% G_p after oxidation for 5h at 1450 °C.

descending trend with increasing time, respectively. Therefore, from the curves in Fig. 11, it can be concluded that the mechanism in the $Zr10G_p$, $Zr15G_p$, $Zr30Si10G_p$, and $Zr30Si15G_p$ samples is parabolic, while in pure ZrB_2, it is linear. For further investigation and confirmation of this matter, the following relationship was used.

$$(\Delta W/S)^n = kt \tag{6}$$

In this equation: ΔW represents the weight change, n is the oxidation exponent, S is the surface area exposed to oxidation, k is the oxidation rate constant, It is the oxidation time.

According to Fig. 11, the calculated values of n were obtained as 1.42, 2.2, 2.07, 2.08, 2.001, 2.03, and 2.1 for Zr, $Zr10G_p$, $Zr15G_p$, Zr15Si, Zr30Si, $Zr30Si10G_p$, and $Zr30Si15G_p$ samples, respectively. If the value of n is equal to 1, it indicates linear behavior, which means the oxidation mechanism is controlled by the reaction. In this case, a thick, unstable oxide layer forms on the surface of the sample due to the reaction of oxygen with the surface of the sample, leading to an increased oxidation rate over time. This mechanism occurs at higher temperatures.

If n is equal to 2, it indicates parabolic behavior, which means the oxidation mechanism is controlled by the diffusion of oxygen. In this case, a thick, stable oxide layer forms on the surface due to the reaction of oxygen with the sample, which resists further oxygen diffusion and results in resistance to oxidation and a decreased oxidation rate over subsequent times. This mechanism occurs at lower temperatures. So, it can be deduced that the oxidation mechanism of approximately all samples (except Zr) is parabolic.

The occurrence of the parabolic mechanism (which indicates better oxidation resistance) in samples containing Gr and SiC compared to pure ZrB_2, which tends to follow a linear oxidation mechanism, can be attributed to the formation of an adherent oxide layer that hinders oxygen diffusion and further oxidation. In contrast, in the pure ZrB_2 sample, the boron oxide layer does not form stably and tends to evaporate, leading to increased oxidation of the sample and resulting in a linear oxidation mechanism.

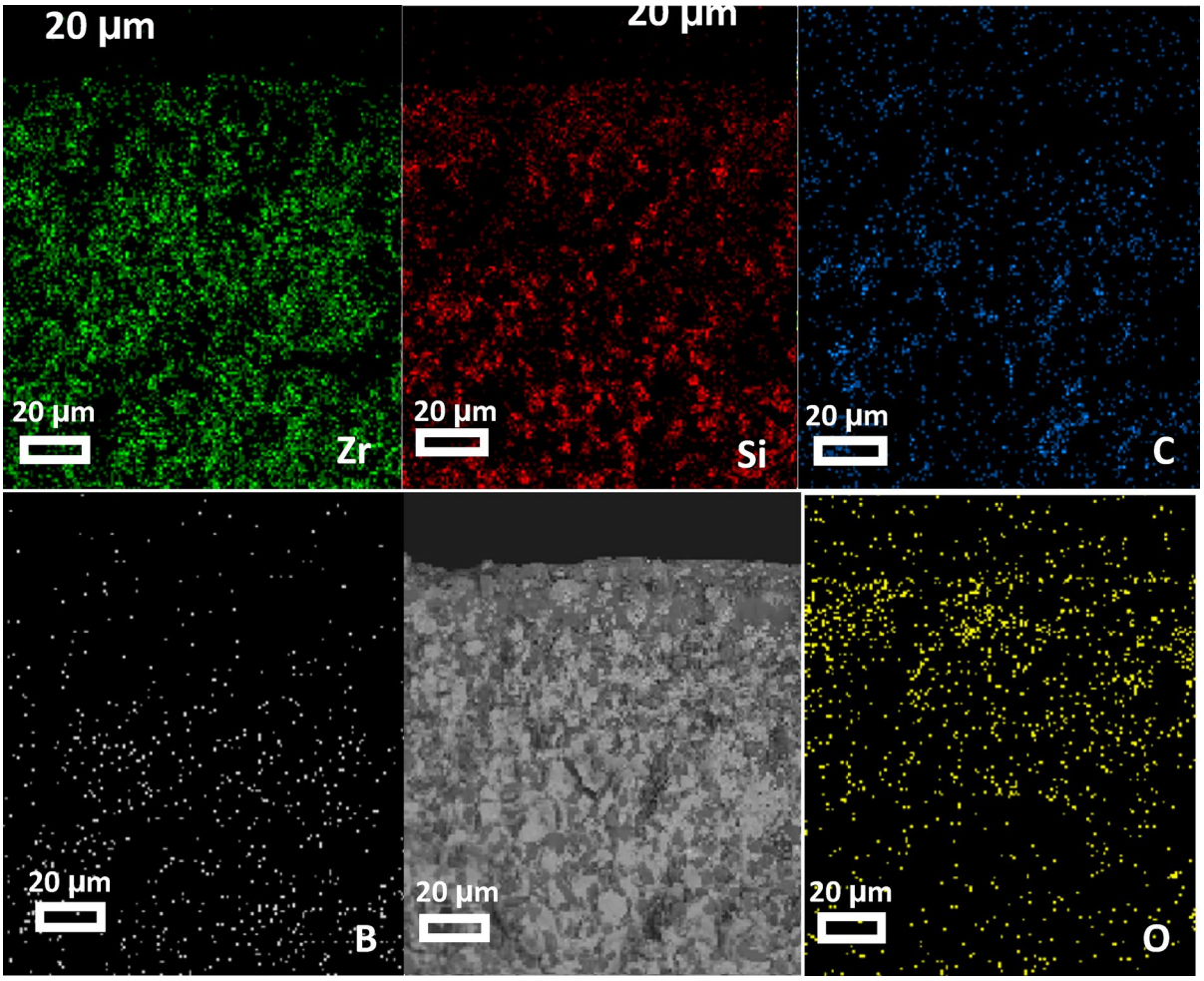

Fig. 9. Map analysis of the cross section of $Zr30Si15G_p$ after oxidation for 5h at 1450 °C, as well as its EDS profile.

Conclusion

Samples containing graphite and silicon carbide, both individually and simultaneously, were fabricated at a temperature of 1850 °C using the SPS method. The investigation of the oxidation resistance of the samples at 1450 °C showed that the addition of graphite and silicon carbide individually significantly improves the oxidation resistance of pure zirconium diboride. Specifically, the thickness of the oxide layer decreased from 129 ± 5 µm in the pure zirconium diboride sample to 112 ± 5 µm, 80 ± 4 µm, 62 ± 5 µm, 38 ± 3 µm, 40 ± 4 µm, and 64 ± 5 µm in the $Zr10G_p$, $Zr15G_p$, Zr15Si, Zr30Si, $Zr30Si10G_p$, and $Zr30Si15G_p$ samples, respectively. This improvement is attributed to the prevention of boron oxide evaporation and the formation of an adherent and oxidation-resistant oxide layer. Additionally, it was found that the simultaneous presence of silicon carbide and graphite in this study, due to the high addition amounts and lack of uniform distribution, resulted in a decrease in oxidation. It was determined that the weight changes are the result of weight loss due to the oxidation of carbon and the evaporation of B_2O_3, and weight gain due to the oxidation of ZrB_2 and SiC.

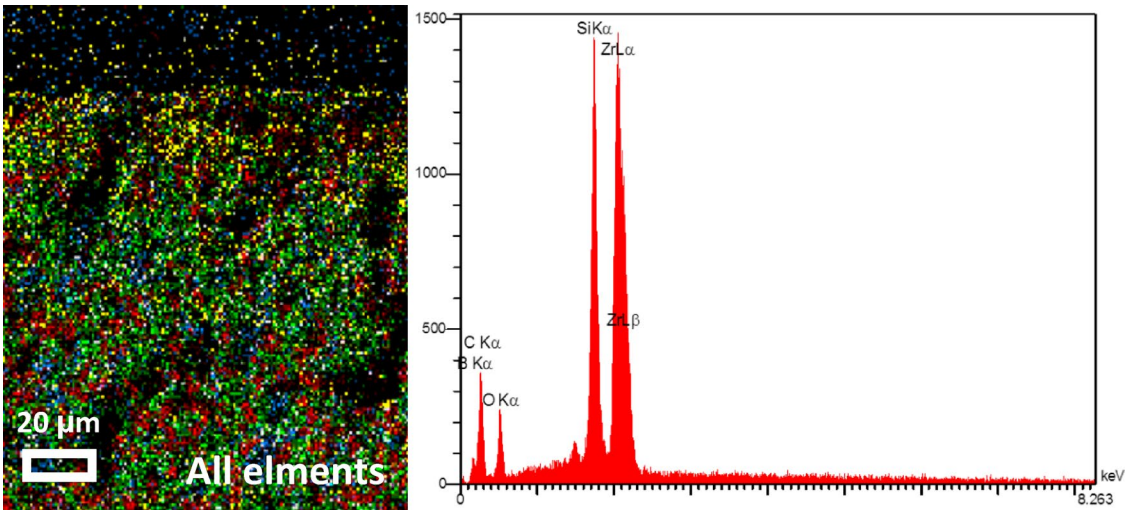

Fig. 9. (continued)

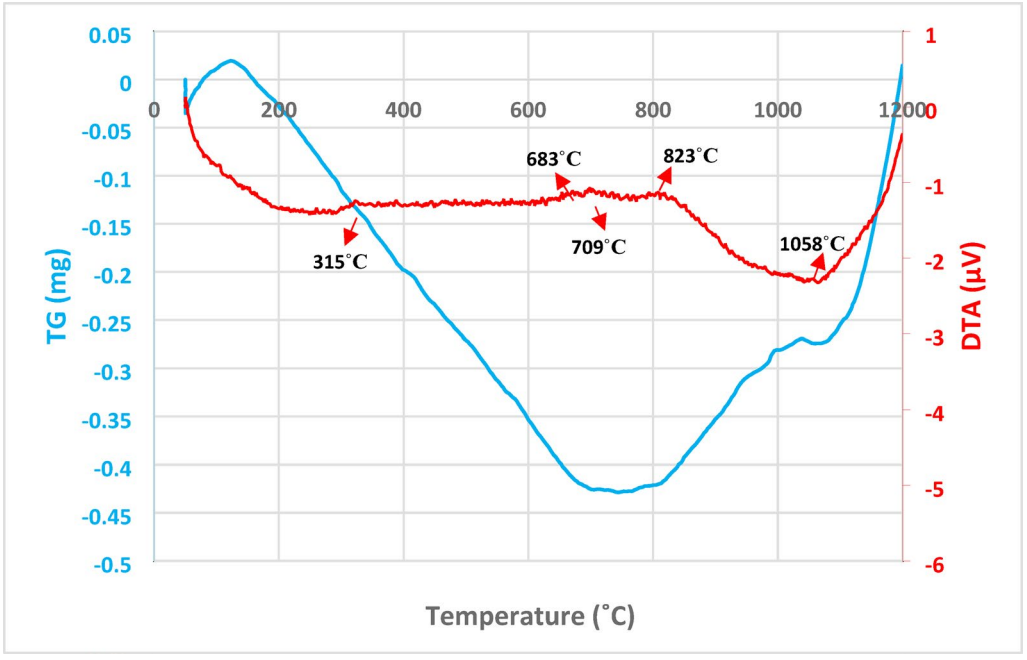

Fig. 10. Mass change and DTA curves of the $Zr30Si10G_p$ sample.

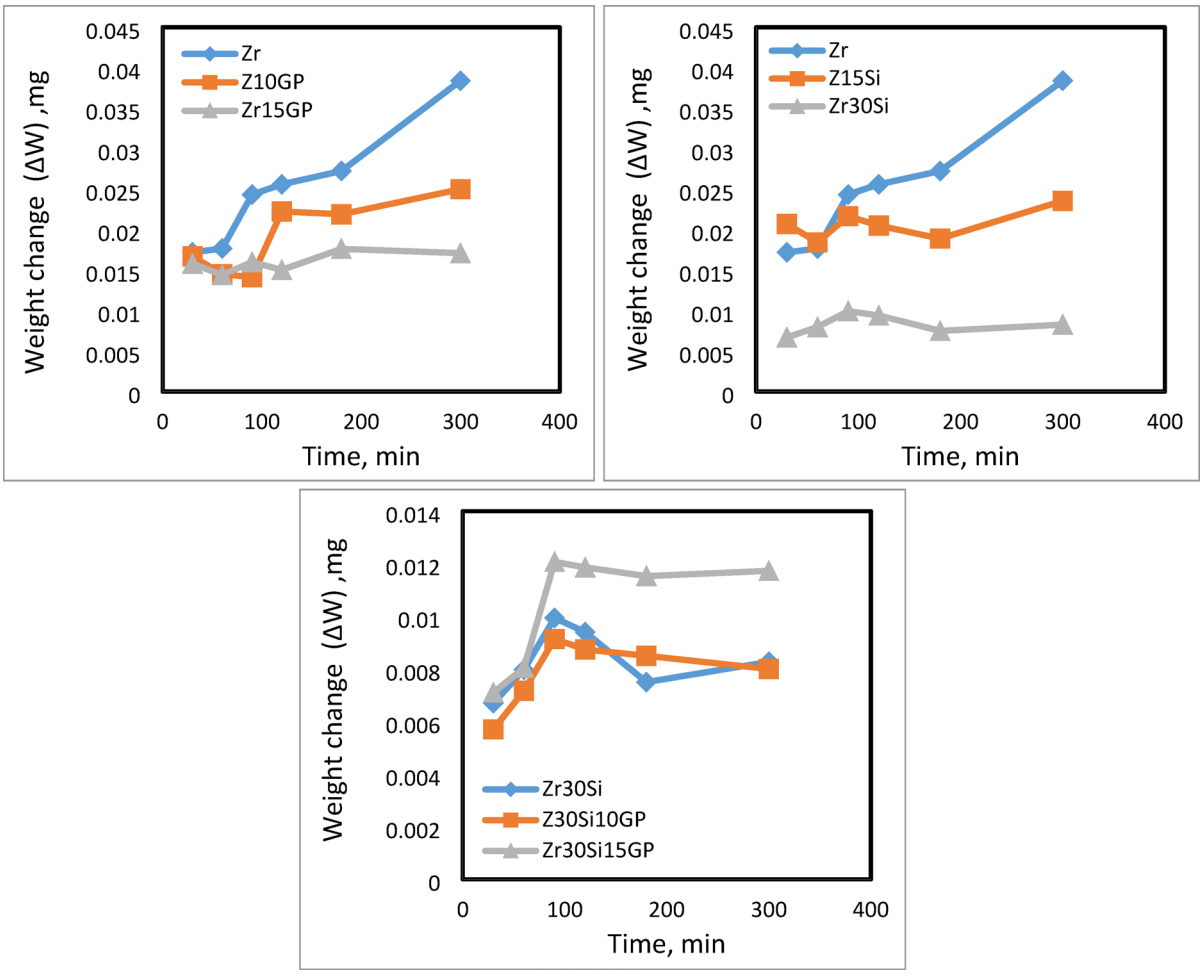

Fig. 11. The weight change curves of all samples against time for oxidation at a temperature of 1450 °C.

Data availability

The data is available on reasonable request from corresponding author (zohre Balak : zbalak@iau.ac.ir).

Received: 12 April 2025; Accepted: 21 October 2025
Published online: 24 November 2025

References

1. Ghasilzadeh Jarvand, M. & Balak, Z. Oxidation response of ZrB_2–SiC–ZrC composites prepared by spark plasma sintering. *Synth. Sinter.* **2**, 191–197 (2022).
2. Shima, A. & Kazemi, M. Influence of TiN addition on densification behavior and mechanical properties of ZrB_2 ceramics. *Synth. Sinter.* **3**, 46–53 (2023).
3. Dodi, E., Balak, Z. & Kafashan, H. Oxidation-affected zone in the sintered ZrB_2–SiC–HfB_2 composites. *Synth. Sinter.* **2**, 31–36 (2022).
4. Parthasarathy, T. A., Rapp, R. A., Opeka, M. & Kerans, R. J. A model for the oxidation of ZrB_2, HfB_2 and TiB_2. *Acta Mater.* **55**, 5999–6010 (2007).
5. Arab, S. M., Shahedi Asl, M., Ghassemi Kakroudi, M., Salahimehr, B. & Mahmoodipour, K. On the oxidation behavior of ZrB_2–SiC–VC composites. *Int. J. Appl. Ceram. Technol.* **18**, 2306–2313 (2021).
6. Rezaie, A., Fahrenholtz, W. G. & Hilmas, G. E. The effect of a graphite addition on oxidation of ZrB_2–SiC in air at 1500 °C. *J. Eur. Ceram. Soc.* **33**, 413–421 (2013).
7. Yang, B.-L. et al. Effect of nano-graphite on mechanical properties and oxidation resistance of ZrB_2–SiC–graphite electrode ceramics. *J. Iron. Steel Res. Int.* **31**, 1502–1513 (2024).
8. Vedel, D. V., Grigoriev, O. N., Mazur, P. V. & Osipov, A. E. Structure, strength, and oxidation resistance of ultrahigh-temperature ZrB_2–SiC–WC ceramics. *Powder Metall. Met. Ceram.* **60**, 60–68 (2021).
9. Silvestroni, L., Failla, S., Neshpor, I. & Grigoriev, O. Method to improve the oxidation resistance of ZrB2-based ceramics for reusable space systems. *J. Eur. Ceram. Soc.* **38**, 2467–2476 (2018).
10. Petry, N.-C. et al. Oxidation resistance of ZrB_2-based monoliths using polymer-derived Si(Zr,B)CN as sintering aid. *J. Am. Ceram. Soc.* **105**, 5380–5394 (2022).
11. Balak, Z. & Azizieh, M. Oxidation of ZrB_2-SiC composites at 1600 °C: Effect of carbides borides, silicides, and chopped carbon fiber. *Adv. Ceram. Prog.* **4**, 18–23 (2018).
12. Asl, M. S. & Balak, Z. Fabrication and characterization of ZrB_2 ceramic in presence of graphite platelet and SiC. *SILICON* **15**, 6911–6919 (2023).

13. Savari, V., Balak, Z. & Shahedifar, V. Influence of graphite platelets with and without SiC on the densification and fracture toughness of ZrB_2 ceramic sintered by SPS. *Carbon Lett.* **32**, 1559–1566 (2022).
14. Chen, H. & Meng, S. High temperature oxidation behavior of ZrB_2-SiC-graphite composite heated by high electric current. *Adv. Mater. Res.* **105–106**, 162–164 (2010).
15. Zhang, X., Hu, P., Han, J. & Meng, S. Ablation behavior of ZrB_2-SiC ultra high temperature ceramics under simulated atmospheric re-entry conditions. *Compos. Sci. Technol.* **68**(7), 1718–1726 (2008).
16. Jin, H., Meng, S., Xinghong, Z., Qingxuan, Z. & Weihua X Oxidation of ZrB_2–SiC-graphite composites under low oxygen partial pressures of 500 and 1500 Pa at 1800 °C. J. Am. Ceram. Soc. 1–7 (2016).
17. Basu, B. Toughening of yttria-stabilised tetragonal zirconia ceramics. *Int. Mater. Rev.* **50**, 239–256 (2005).
18. Manab Mallik, K. K. R. & Mitra, R. Oxidation behavior of hot pressed ZrB_2–SiC and HfB_2–SiC composites. *J. Eur. Ceram. Soc.* **31**, 199–215 (2011).

Author contributions

Zohre Balak conducted the conception, measurements, manuscript composition, and writing, revised the manuscript and validated the data. Hamze Ghanbari Nezhad conducted the experimental design and measurement.

Declarations

Competing interests

The authors declare no competing interests.

Additional information

Correspondence and requests for materials should be addressed to Z.B.

Reprints and permissions information is available at www.nature.com/reprints.

Publisher's note Springer Nature remains neutral with regard to jurisdictional claims in published maps and institutional affiliations.